Aerodynamic Flow Control of a Moving Axisymmetric Bluff Body

Thomas J. Lambert*, Bojan Vukasinovic† and Ari Glezer‡
Woodruff School of Mechanical Engineering,
Georgia Institute of Technology, Atlanta, GA 30332-0405

The present experiments focus on active fluidic control of the aerodynamic forces and moments of an axisymmetric bluff body platform in time-periodic sinusoidal pitch oscillations at reduced frequencies $0 < k < 0.259$. The platform is wire-mounted on a six degree of freedom traverse where each of the eight support wires is individually controlled by a servo motor with an integrated in-line load cell for feedback control of the platform's motion. The aerodynamic forces and moments on the platform are manipulated by controlled interactions of an azimuthal array of synthetic jet actuators on its aft segment with the local cross flow to induce partial (azimuthally-segmented) flow attachment that is coupled with vectoring of its near-wake. The actuation-induced forces and moments can either increase or diminish the corresponding pitch-induced baseline aerodynamic forces and moments. These actuation effects are exploited for open-loop control to suppress or augment the pitch-induced moment, and effect robust (in excess of 50%) control authority over a broad range of oscillation frequencies (up to reduced frequency of 0.259) that are suitable for trajectory stabilization and steering in free-flight.

Nomenclature

A_j	actuator orifice cross-sectional area
c	body chord length
C	transformation matrix in controller
C_D	coefficient of drag
C_p	coefficient of pressure
C_μ	jet momentum coefficient
D	axisymmetric body diameter
D_s	support wire diameter
f	body pitching frequency
f_{cycle}	synthetic jet frequency
F_A	total aerodynamic force
F_D	aerodynamic drag force
F_G	gravitational force
F_L	aerodynamic lift force
F_I	total inertial force
F_W	aerodynamic wire drag force
h_s	body backward-facing step height
k	model reduced frequency
m_n	angle coordinate of n^{th} wire
M	controller motor forces and displacements
M_{BOT}	bottom jet modulation command
M_{TOP}	top jet modulation command
M_p	aerodynamic pitching moment
R_c	Coanda surface radius
Re_D	Reynolds number
St_{act}	actuation Strouhal number
t	time
T_n	Tension measured in n^{th} wire
u_x	streamwise velocity component
u_z	cross-stream velocity component
U_j	maximum jet expulsion velocity
U_0	free stream velocity
W	wire direction matrix
x	streamwise coordinate
x_m	center of body wire mounts
X	controller body forces and displacements
y	side-stream coordinate
z	cross-stream coordinate
α_x	roll coordinate
α_y	pitch coordinate
α_z	yaw coordinate
ΔF_D	actuator induced drag force
ΔF_L	actuator induced lift force
$\Delta F_{L,BOT}$	bottom actuator induced lift force
$\Delta F_{L,TOP}$	top actuator induced lift force
ΔM_p	actuator induced pitching moment
ρ	air density
ζ	planar vorticity
τ	body oscillation period
τ_{conv}	body convective time scale
τ_{cycle}	synthetic jet period

* Graduate Research Assistant, AIAA Member.
† Research Engineer, AIAA Member.
‡ Professor, Associate Fellow AIAA.

I. Technical Background

The present work focuses on the manipulation of separated flows over external aerodynamic platforms with the objective of exploiting the aerodynamic forces and moments that result from partial or full flow attachment for platform steering and stabilization. The separating shear layer over stalled 2- and 3-D aerodynamic surfaces is typically dominated by a strong coupling to the instability of the near wake (e.g., Wu et al.[1]). One type of separation control strategy uses coupling to the narrow-band receptivity of the separating flow at unstable Strouhal numbers of the near wake (St_{act} ~ O(1), e.g., Hsiao et al.[2], Neuberger and Wygnanski[3], Chang et al.[4], Williams et al.[5], and Seifert et al.[6]). Another strategy decouples global flow instabilities from fluidic modification of the "apparent" aerodynamic shape with actuation frequencies that are at least an order of magnitude higher than the flow frequency (e.g., Erk[7], Smith et al.[8], Amitay et al.[9], Honohan et al.[10], Glezer et al.[11]).

Active control of flow separation and thereby of global aerodynamic performance can be significantly enhanced by hybrid, active and passive control that exploits the interaction of the actuation jets with adjacent solid surfaces or the Coanda effect that has been investigated extensively since the 1940s (e.g., Newman[12]). The Coanda effect has been the basis of circulation control over lifting surfaces in numerous aerodynamic systems (e.g., Englar[13]). A passive feature that can be used is a sharp leading edge to induce separation of an axisymmetric body that was controlled by jet injection further downstream[14]. Hybrid flow control was also demonstrated by Nagib et al.[15] who combined a short backward facing step with a jet to control local separation. This approach was also utilized for controlling internal flows, for example, by Lo et al.[16] who controlled separation in adverse pressure gradients in a diffuser.

Because the Coanda effect is associated with the attachment of an inherently separated flow to a solid surface, this flow configuration presents a unique opportunity to create net aerodynamic forces on various bluff bodies through controlled activation. Freund and Mungal[17] reduced the aerodynamic drag of axisymmetric bodies by up to 30% using induced attachment at the aft corner of the body by steady, circumferentially-uniform blowing over Coanda surfaces. Rinehart et al.[18,19] demonstrated generation of a asymmetric force on an aerodynamic platform using the interaction of a single synthetic jet with an integrated axisymmetric azimuthal Coanda tail surface along a backward facing step. In a related investigation, McMichael et al.[20] exploited this flow control approach to the separated base flow of an axisymmetric 40 mm spin stabilized projectile to effect aerodynamic steering forces and moments that were sufficient to control the trajectory of the projectile in flight. Corke et al.[21] reported alteration of the drag and side forces on an axisymmetric body using tangential plasma actuation placed upstream of a Coanda surface. Abramson et al.[22,23] extended the Coanda actuation methodology to effect prescribed (asymmetric) side forces by using four individually-controlled azimuthally distributed synthetic jets within the rearward facing step of the tail and demonstrated that the induced forces can be used to effect steering during flight and trajectory stabilization. Finally, Lambert et al.[24,25] showed that unstable motion of a free-moving axisymmetric model can be significantly suppressed or enhanced with appropriate timing and modulation of the actuation, and this could lead to significant directional control authority for free flight aerodynamic bodies.

Control of the aerodynamic forces on axisymmetric airborne platforms builds on numerous earlier investigations of the uncontrolled baseline flow and its natural instabilities. The basic motions of spinning projectiles, including natural nutation and precession linear and nonlinear instabilities, induced by Magnus, damping, and normal forces and moments are discussed in detail in the classical work of Nicolaides[26]. The instabilities of symmetric projectiles in the presence and absence of spin were discussed in detail by Murphy[27]. While spin-stabilized projectiles are gyroscopically stable to axisymmetric moment instability, they are susceptible to roll resonance[28], and spin-yaw lock in[29], which add complicated non-linear effects to the projectile dynamics that are in general hard to correct for. In recent years considerable attention has been devoted to the development active control approaches for both fin- and spin-stabilized projectiles, including aerodynamic forces induced by a piezoelectric-articulated nose section[30], synthetic jet actuation on a spinning projectile[31], and the swerve response of finned and spin-stabilized projectiles to generic control forces[32,33].

An inherent problem with any experimental aerodynamic study of a nominally 'free' body is related to its mounting into a test section. Ideally, the model support should not cause aerodynamic interference (e.g., magnetic-force supports[34]), but the most predominant supports involve sting mounts that are directly in the body's wake. An alternative support, aimed at minimizing the wake-support interference, was utilized by Abramson et al. [22,23] and Lambert et al.[24], where a model is supported by thin wires. The current work takes advantage of a thin wire mounting setup in order to create a novel traverse, and the goal of the present investigation is to assess the effect of hybrid flow control on a dynamic axisymmetric body.

II. Dynamically-Controlled Wire Support System: Experimental Setup and Procedures

The present investigation is conducted in an open-return wind tunnel at Georgia Tech having a test section that measures 91 cm on the side with a test section speed of up to U_0 = 40 m/s. The model diameter is 90 mm (Re_D up to $2.4 \cdot 10^5$), and is shown in Figure 1a and b from the side and back, respectively. The aerodynamic control forces (and associated moments) on the projectile model are generated using an azimuthal array of four independently-driven synthetic jet actuators that are equally distributed along the perimeter of the tail section, with primary importance placed on the two actuators within the plane of the model pitching motion. Each jet is embedded into the surface with an area A_j = 0.38×34.3 mm^2 rearward facing orifice such that it is issued over a Coanda surface formed by an azimuthal segment of an axisymmetric constant radius of R_c = 12.7 mm. The jet actuation leads to the partial attachment of the outer flow along the Coanda surface resulting in a reaction force by the turning of the outer flow into the wake region. The axisymmetric model is built using both stereo-lithographed and aluminum components and measures D = 90 mm in diameter and c = 165 mm in length. Eight mounting wires are fixed into the center aluminum piece, and the rest of the model containing the synthetic jet actuators is fastened together to the center with an aluminum spine that extends through the model. The rear component with the Coanda surface has the cut-in grooves along the orifice edges that guide the jet flow and prevent its spanwise diffusion. The adjoining backward-facing step to the circumference of the body is h_s = 1.5 mm in height. The step height was chosen such that it is shallow enough to enable local flow attachment when the control jet is activated, but deep enough to prevent attachment of the free stream flow in the absence of the jet actuation.

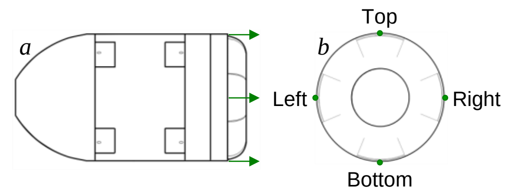

Figure 1. *Side (a) and upstream (b) views of the centered wind tunnel model with four hybrid fluidic actuators marked in green.*

The experimental axisymmetric model along with the traverse support are shown in Figure 2. The D_s = 0.96 mm support steel wire is selected to be thin enough to reduce the drag coefficient and decouple its vortex shedding from the model, while thick enough to minimize translational and rotational vibrations. Each wire that extends from the model is fastened to a servo motor, with an in-line load cell, and each motor is fastened to an external spring for pretension. The electrical connection for the actuators is enabled by means of the wires weaved along the back four support wires and through the tunnel walls, while the support wires provide the electrical ground. The servo motors are controlled through analog outputs from a *Quanser Q*8 boards that are controlled through *QuaRC* hardware-in-loop commands in a *Simulink* controller, and the actuation is controlled through external amplifiers controlled by a secondary *Q*8 board. The servo motors are chosen such that they can induce a displacement ranges on the order of 50 mm and 10° in each direction, and provide high frequency motion of up to f = 50 Hz with smaller displacement. These motions were chosen from time scales and deflection scales on the order of previously measured aerodynamic instabilities (20 ms, 10°) that were found in a single degree of freedom model by Lambert et al[25]. The *FUTEK* in-line load cells were chosen to resolve forces on the order of the expected synthetic jet actuation forces of 0.6N. The load cells were calibrated over the entire range through attaching individual weights, and the calibration was verified by placing static weights on the model and resolving the known lift force. The springs were chosen to give a pretension of 50 N, initializing each wire to half of its allowed tension range.

The final component to the wire support system is an external six degree of freedom *Vicon* motion analysis system. A representation of this system is shown in Figure 3. The system is comprised of six MX-T40S cameras, each with a 12.5 mm lens, capable of capturing 4 megapixels of information with a response rate of 515 frames per second at full

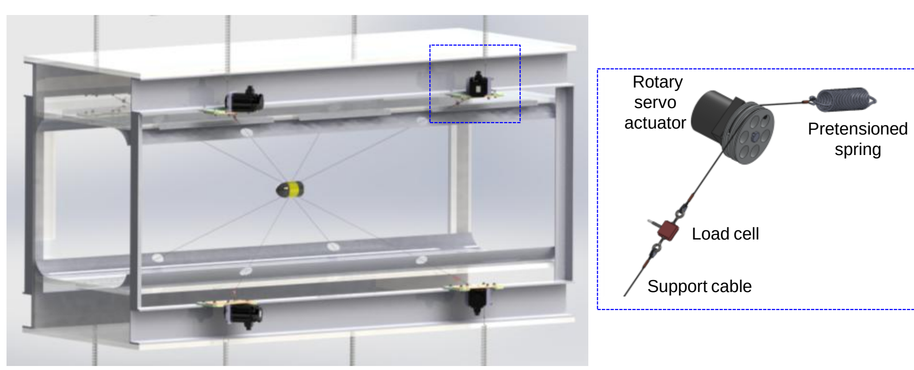

Figure 2. *Six degree of freedom traversing mechanism utilizing eight support wires, each connected to an in-line load cell, a servo-actuator, and a pre-tensioned spring.*

resolution. The cameras record IR reflections off of thin markers (minimum of six) placed on the aerodynamic platform and uses these markers to calculate the displacement of the model in six degrees of freedom. An external MX-Giganet core unit synchronizes the cameras and transfers the data to a separate computer that then interprets the camera input and broadcasts a data stream of the model's motion through UDP protocol at 500 Hz.

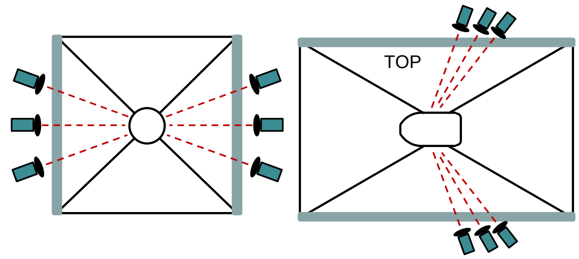

Figure 3. *Front and top views of the motion analysis system.*

III. Six Degree of Freedom Controller Design

The fundamental description of the system is as follows: There is an over-constrained model to be controlled in six output degrees of freedom (x, y, z, α_x, α_y, α_z), to which there are eight input motor angles (m_1, ..., m_8). We define x as streamwise, y as side-stream, z as cross-stream, α_x as roll, α_y as pitch and α_z as yaw. The model has an inertial force and moment (F_I), an aerodynamic force and moment (F_A), and a gravitational force and moment (F_G) acting on it. In addition, each mounting cable has a tension (T_1, ..., T_8) that is dependent on the forces on the body, as well as the motor angles. Each motor shaft has a certain amount of inertia and damping, and each wire is assumed to have an aerodynamic force that is entirely a form drag, with negligible inertial force or friction drag. The mounting locations of each of the centers of the motor pulleys are known, along with the corresponding pulley radii. The mounting locations of each of the wires in the body are also known relative to the center of the model mounts (x_m = 0.54c from the nose). The wires are not assumed incompressible, but each one is assumed to compress only as a spring with known elastic modulus and cross-sectional area.

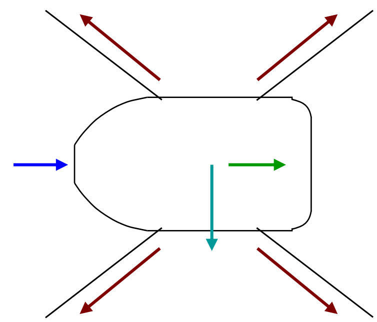

Figure 4. *Free body diagram of the aerodynamic platform using aerodynamic (blue), tension (red), gravitational (cyan) and inertial (green) forces and moments.*

In order to build a functional controller, there needs to be stable real-time solutions to two problems: the first is a calculation of the model orientation (x, y, z, α_x, α_y, α_z, and all components of F_A) given the motor orientation (m_1, ..., m_8, T_1, ..., T_8), where all values at the previous time step and all geometric variables are allowed to be used. To fully define the six degree of freedom coordinate system, a yaw first, pitch second, and roll last rotational convention is adopted. In order to accurately model the traverse motion, the first function that is required is the direction of each mounting wire given the motor positions, model position, and wire tensions from the frame of the aerodynamic model shown in Eq. 1:

$$\begin{pmatrix} W_{x,n} \\ W_{y,n} \\ W_{z,n} \end{pmatrix} = function\left(x, y, z, \alpha_x, \alpha_y, \alpha_z, m_1, \ldots, m_8, T_1, \ldots, T_8, and\ Mechanical\ Constants\right) = \overleftrightarrow{W_{3x8}} \quad (Eq. 1)$$

The second function that is required is a relation between the wire tensions and the force on the model. This is done with a force and moment balance with the inertial, gravitational, and aerodynamic forces and moments with the wire tension, as shown in Figure 4. The gravitational force and inertial force are entirely dependent on the orientation of the model, and independent of the orientation of the wires. This allows Eq. 1 to be reorganized as shown below in Eq. 2:

$$\vec{X} = \begin{pmatrix} x \\ y \\ z \\ \alpha_x \\ \alpha_y \\ \alpha_z \\ F_A \end{pmatrix} = \overleftrightarrow{C}_{12x16} * \begin{pmatrix} m_1 \\ \ldots \\ m_8 \\ T_1 \\ \ldots \\ T_8 \end{pmatrix}, \quad where\ \overleftrightarrow{C} = function(\overleftrightarrow{W}, Mechanical\ constants, and\ time) \quad (Eq. 2)$$

The formulation of variables and constants as shown in Eq. 2 is powerful because it separates forces and displacements of the model ($\vec{X}$), with the forces and displacements on the motors ($\vec{M}$). The transformation matrix between these two quantities ($\overleftrightarrow{C}$) depends on the orientation of both $\vec{M}$ and $\vec{X}$ and therefore must be reevaluated at each time step, where the current controller linearizes this calculation to optimize runtime and allow the controller to operate at 1 kHz. The inverse calculation from the model coordinates to the motor coordinates is also quickly computed with a least norm matrix inverse solution.

A depiction of the controller is shown as a block diagram in Figure 5. The commanded position is specified to the controller as a six-vector, and it is compared with the measured position estimate determined from the load cells and motor encoders. This comparison is used to calculate an eight-vector of desired motor positions, and the motor command is then generated from the desired motor positions using PID control. The motors then effect the model dynamics, which is then interpreted by the encoders and load cells, thus closing an 'inner loop' control. The load cell and encoder readings, as well as the estimated aerodynamic forces and model positions are recorded for data analysis. Independent synthetic jet commands can be defined by the user trigger relative to the desired motion, and the effect that the jets have on the aerodynamic forces and model motions are measured through the encoders and load cells as well. In addition, the motion analysis system is set up and calibrated for a much more accurate measurement of the model motion response, and is incorporated into the controller as an 'outer loop' which is used to modify the motor commands to minimize the error between the desired motion and the recorded motion in the camera system, which is done with a secondary PID control.

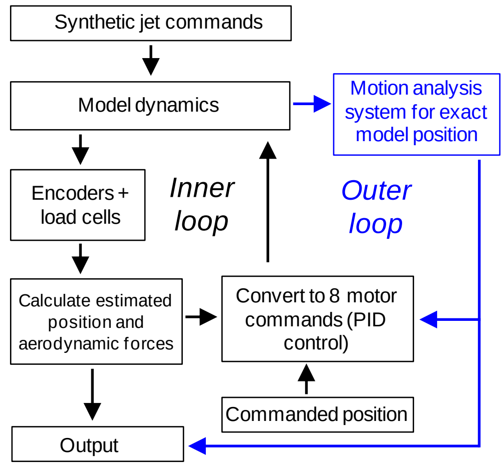

Figure 5. *Schematics of the controller.*

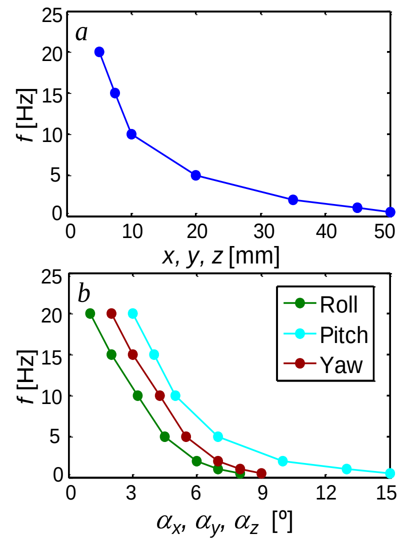

Figure 6. *Variation of displacement range with frequency for translational (a) and rotational (b) motions.*

The system dynamic performance is characterized in terms of displacement range and frequency of sinusoidal commands and is depicted in Figure 6. The displacement amplitude is 50 mm plunge (x, y, and z), 8° α_x, 9° α_z, and 15° α_y at f = 0.5 Hz, and decreases to 5 mm (x, y, and z), 1° α_x, 2° α_z, and 3° α_y at f = 20 Hz. The range of motion decreases with frequency of motion because the inertial force grows proportional to the acceleration of the system, and increases the required torque of the motors at higher frequencies. This larger torque requires the tension in the mounting wires to increase with the same motion range, and because the load cells are limited to 110 N of tension, the range of the motion of the system has to decrease. The variation of the range of the model with the frequency of the motion is shown in Figure 6a for translational motion, and Figure 6b for rotational motions. The choice of the wire mounting location does not affect the translation range, but does affect the angular range, and these locations are chosen to maximize the range of pitch while still having significant authority in roll and yaw.

IV. Aerodynamic Response of the Centered Body

Before examining the model dynamics, a study was conducted to assess the synthetic jet control authority on generation of aerodynamic forces and moments on the axisymmetric body held stationary at the central position. This effect has been studied previously by McMichael et al.[20], Abramson et al.[22,23], and Lambert et al.[24], with a computational model, fixed model with reaction forces, and dynamically-enabled model with reaction forces, respectively.

Initially, a study of the drag of the model is conducted on the body held at center. The drag force was measured over a range of wind tunnel speeds as F_D. The expected wire drag is calculated treating the wires as cylinders with flow over them of the projected wind speed across the cylinder F_W. The value of the extracted platform drag $(F_D - F_W)$ is plotted against the dynamic pressure multiplied by the platform cross-sectional area to resolve a coefficient of drag (C_D) of 0.238, with good agreement with the expected C_D of 0.25 from Hoerner[35], as shown in Figure 7. The rest of the current investigation is conducted at the fixed free stream speed of U_0 = 40 m/s.

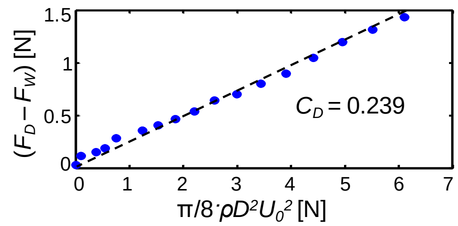

Figure 7. *Measured model drag (●) with scaled tunnel speed and a linear fit yielding the measured drag coefficient.*

Next, the effects of the hybrid actuators are investigated with the jet momentum coefficient set to $C_\mu = (U_j^2 \cdot A_j)/(U_0^2 \cdot \pi D^2) = 3 \cdot 10^{-3}$, and the actuation cycle frequency set to f_{cycle} = 1.4 kHz (τ_{cycle} = 0.7 ms). When the synthetic jets are inactive, the model experiences separation off of each of the backward facing steps on the aft end of the model, and the jet actuation leads to the partial attachment of the outer flow along the Coanda surface resulting in a reaction force by the turning of the outer flow into the wake region. This vectored wake induces a reaction force and moment on the model, which is shown in Figure 8. The moment on the body throughout this work is measured relative to mounting center of wires on the body at x_m. The response of a single actuator measured by the load cells is shown in Figure 8a,b, and c, showing the actuator induced forces, ΔF_D = 0.03N and ΔF_L = 0.6 N, and the actuator induced moment, ΔM_P = 0.008 Nm, which is in good agreement with previous studies by Abramson et al.[2,3], and Lambert et al.[5]. When both jets are activated, the effect of the jets in ΔF_L and ΔM_P is canceled out (Figure 8d and e), while the actuator induced drag is approximately doubled to ΔF_D = 0.06N (Figure 8f).

To understand the actuation-induced wake development while the axisymmetric model is centered, different actuation schemes are applied and the resulting flow fields are investigated with planar PIV. Figure 9 shows the ensemble-averaged flow field (based on 300 individual flow realizations) in terms of the mean velocity field vectors overlaid on a raster plot of the mean vorticity, ζ, at the central vertical plane of the model. Figure 9a shows the model wake without flow control, having expected symmetry about the body's axis. Although the flow field is axisymmetric (in a time-averaged sense), the upper and lower shear layers have a different sense of ζ due to the Cartesian coordinate system utilized in the measurement plane for calculating ζ. Figure 9b shows the model wake with the top jet actuated, deflecting the wake downwards across the centerline and inducing a large asymmetry while decreasing the extent and magnitude of the region of ζ near the jet. This wake deflection causes a reaction on the model with positive ΔF_L and negative ΔM_P, as shown in Figure 8b. Figure 9c, showing both jets activated, causing the extent and magnitude of the region of ζ near each jet to decrease, and vectors the wake on

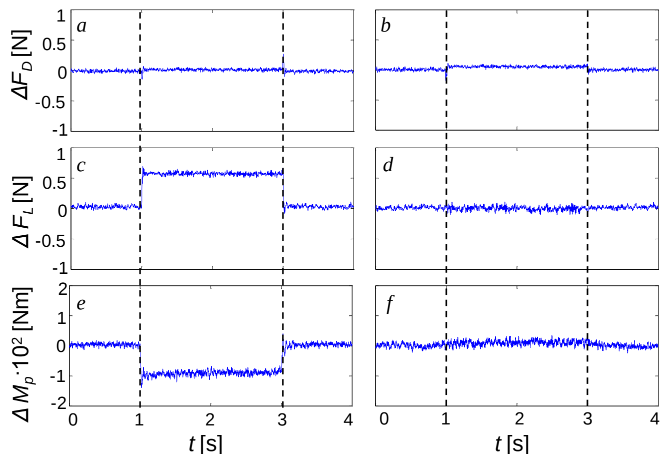

Figure 8. *Actuator induced drag (a,b), lift (c,d), and pitch moment (e,f) for one (a,c,e) and two (b,d,f) jets activated at $C_\mu = 3 \cdot 10^{-3}$ with jet onset and termination shown by dotted lines.*

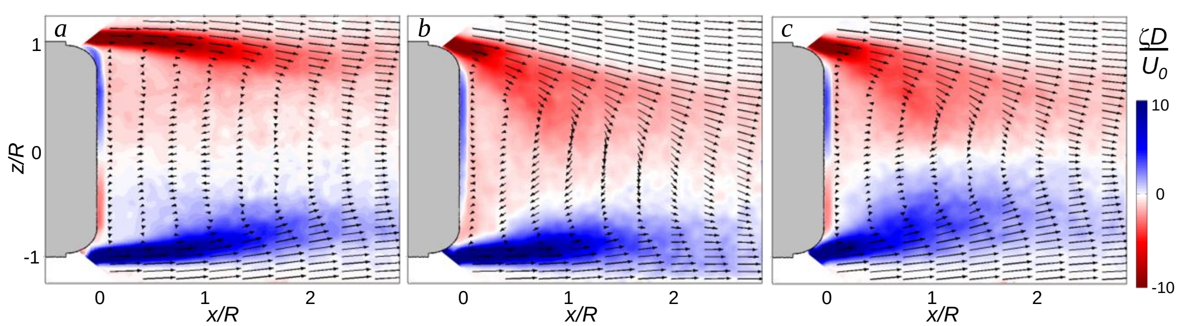

Figure 9. *Raster plots of the mean vorticity field with overlaid mean velocity vectors for a static model at $\alpha_y = 0°$ for the baseline (a), and the flows actuated by the top (b), and both top and bottom (c) jets at $C_\mu = 3 \cdot 10^{-3}$.*

both side closer to the center, closing the wake. Because this flow field is again symmetric, there is no ΔF_L or ΔM_P on the model, and the ΔF_D seen in Figure 8f can be attributed to the change in shape and magnitude of the wake velocity outside of the controlled perimeter.

V. Aerodynamic Response of the Moving Bluff Body

Once the centered model response has been assessed, the main investigation focuses on commanding a dynamic response from the body. The remainder of the present work focuses on sinusoidal pitch commands for the model motion. Figure 10 shows the measurement of the lift induced on the model commanded for sinusoidal pitching at f = 1 Hz (a reduced frequency of $k = \pi cf/U_0 = 0.013$), and an amplitude of 3°. The force and moment traces presented here are the average of 100 seconds of data for noise suppression. The recorded lift force variation with pitching angle (F_L vs. α_y) is plotted in Figure 10a, and the pitching moment trace (M_P vs. α_y) is shown in 10c. It is notable that both F_L and M_P increase with increasing α_y. In addition, a secondary traverse command is implemented with the same motion of the model with the top jet continuously actuated, where lift force induced solely by the actuation is plotted with pitching angle (ΔF_L vs. α_y) in Figure 10b, and the actuator induced pitching moment trace (ΔM_P vs. α_y) is shown in 10d. Activation of the top actuator in Figures 10b and d vectors the wake downwards towards the center, causing a reaction force on the model with positive ΔF_L and negative ΔM_P, where the magnitude of the ΔF_L and ΔM_P depends on α_y. Because F_L and M_P have the same sense and ΔF_L and ΔM_P have the opposite sense, actuation chosen to decrease F_L throughout the pitching cycle consequently increases M_P. It is observed that the maximum magnitude of induced ΔF_L = 0.9N and ΔM_P = -0.01Nm by the top actuator occurs when the model is pitched down to α_y = -1°, which is attributed to the geometry of the backward facing step, and the respective flow field on the model's aft end. The present range of body orientations had been investigated prior by Lambert[24] with the model held at a static angle of attack. In that work, F_L, ΔF_L and ΔM_P were recorded, and they are plotted in Figure 10a, c, and d in solid symbols. There is a small deviation in the ΔF_L and ΔM_P past the maximum values at α_y < -1°, but the agreement is very strong everywhere outside of this region. In addition, the center of pressure (C_p) of the centered model is known to be about x/c = 0.24 upstream of x_m, and the expected moment on the model ($F_L \cdot C_p$) is plotted in Figure 10c in black. This measured moment has more hysteresis than the expected moment due to variations in the Cp over the cycle.

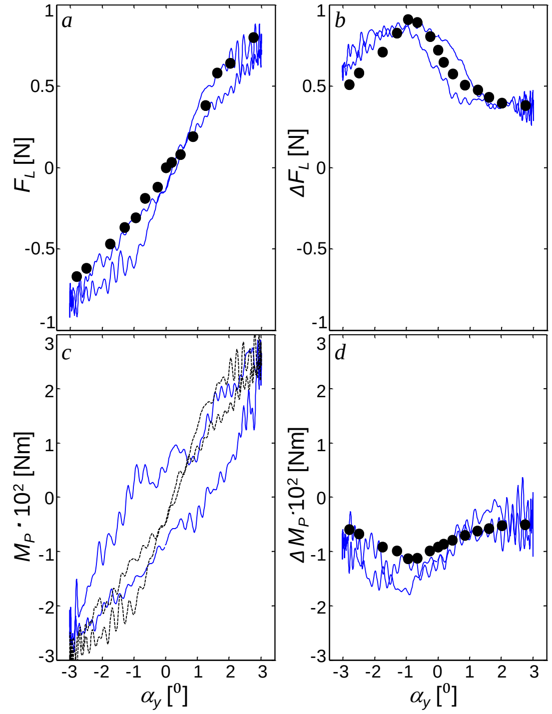

Figure 10. *Motion induced lift (a) and moment (c), and actuation induced lift (b) and moment (d), as well as the expected moment using the known center of pressure on the centered model (-). Prior results on a static model by Lambert et al.*[24] *(●) are shown for reference.*

The primary emphasis of the current work is to assess the control authority of hybrid actuators on the present model when it is dynamically pitching. An important aspect of flow control implementation in dynamic configurations is the frequency response of both the hybrid actuators and the baseline flow. The onset of actuation induces a ΔF_L and ΔM_P response that acts like a step function with a rise time of about 20 ms (50 Hz), as shown in Figure 8, with the magnitude of ΔF_L and ΔM_P on α_y as well as its rate, $\dot{\alpha}_y$. The frequency response of the baseline flow is analyzed using representative samples of f = 1, 5, 10, and 20Hz (k = 0.013,0.065,0.130, and 0.259, respectively) that span a range from pseudo-steady to quasi-unsteady frequencies, shown in Figure 11. The emphasis of this investigation is on using actuation for steering and stabilization of an airborne model in pitch motion, and therefore the rest of this work places emphasis on the lift force trace, F_L vs. α_y, and pitch moment trace, M_P vs. α_y. Furthermore, as the pitch motion is detected as representative for the flow control assessment, only two control jets are utilized in the remaining sections of the paper, namely the top and bottom jets. Figure 11a and e show F_L vs. α_y, and M_P vs. α_y, respectively, of the model pitching at k = 0.013, as the 'low' frequency representative, which was shown to be in agreement with previous static data in Figure 10a and c. Figure 11b and e show the

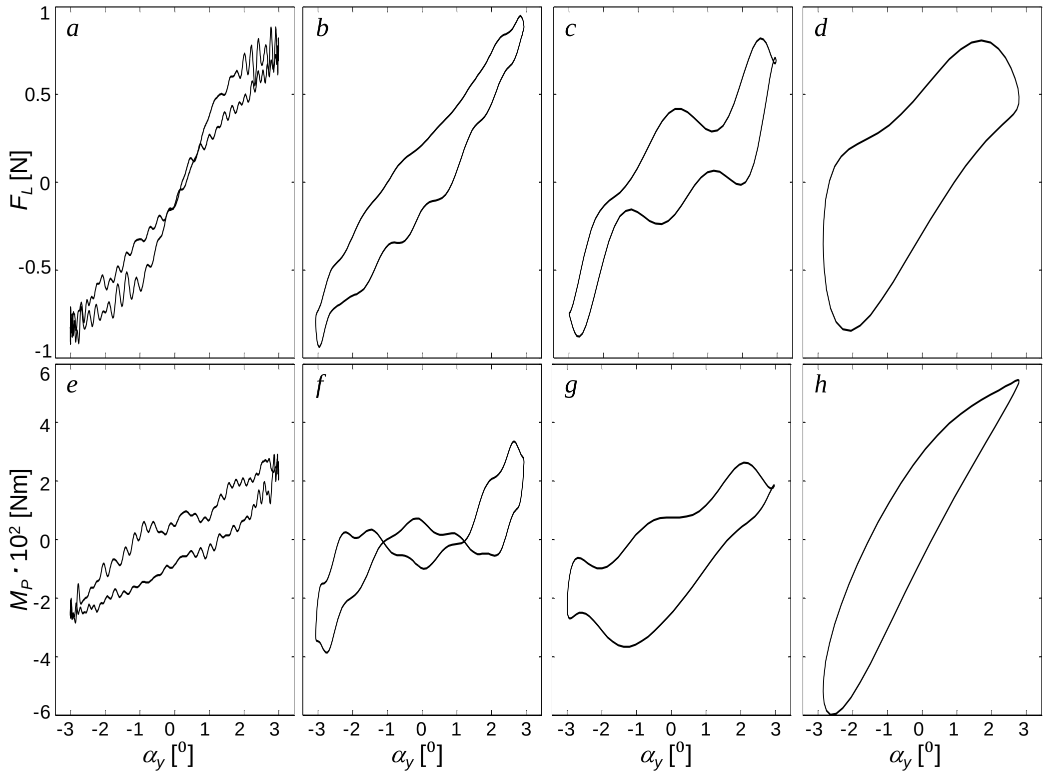

Figure 11. *Motion induced lift (a–d) and moment (e–h), development with pitch angle, α_y, at reduced frequencies k = 0.013 (a,e), 0.065 (b,f), 0.130 (c,g), and 0.259 (d,h).*

change in the F_L vs. α_y and M_P vs. α_y for $k = 0.065$, where the peak values of F_L remain similar, yet the corresponding peak values of M_P increase. In addition, the path and hysteresis of both F_L vs. α_y and M_P vs. α_y are also altered. This pattern continues through $k = 0.13$, shown in Figure 10c and g, and the 'high' frequency representative, $k = 0.259$, shown in Figure 10d and h, where the F_L peaks remain unaltered (compare Figures 11a-d), and the M_P peaks increase (compare Figures 11e-h). The F_L vs. α_y and M_P vs. α_y paths and hysteresis vary notably with k, and therefore an actuation has to be tailored to effectively address the baseline response of the k of interest, as discussed below in Section VI.

To understand the baseline wake development of the dynamic model during oscillation at different k cycles, the phase averaged flow field is measured in a similar style to the time averaged flow field in Figure 9. Figure 12 shows six phase-averaged flow fields (based on 300 individual realizations) in terms of the velocity field vectors overlaid on a raster plot of ζ, at the central vertical plane of the model for $k = 0.013$ ($\tau = 1$s, Figure 12a-f), and $k = 0.259$ ($\tau = 50$ms, Figure 12g-l). The baseline cycle is symmetric regardless of frequency, therefore the phases chosen for brevity are representative for the first half cycle: $t/\tau = 0$ (Figure 12a and g), 0.083(Figure 12b and h), 0.167(Figure 12c and i), 0.25(Figure 12d and j), 0.333(Figure 12e and k), and 0.417(Figure 12f and l). The model pitching angle corresponding to these phases is $\alpha_y = 0^o$, 1.5^o, 2.6^o, 3^o, 2.6^o, and 1.5^o, respectively. In both Figure 12a-f and Figure 12g-l, the shear layer follows the model, and in both Figure 12a and Figure 12g, the shear layer is not centered when the model is at center, due to the wake lagging the model by a function of the convective time scale ($\tau_{conv} = D/U_0 = 2.25$ ms). However, this time scale is a much larger portion of the cycle when the model is moving faster, leading to much more asymmetry in Figure 12g than in Figure 12a, which is also commensurate with the increase in F_L vs. α_y, and M_P vs. α_y hysteresis with k shown in Figure 11. In Figure 12a, the wake ζ is predominantly counterclockwise, while, as it starts to pitch up $t/\tau = 0.083$ in Figure 12b, the wake is dominated by the clockwise sense of ζ for the remainder of the pitch up cycle. In contrast, for $k = 0.259$, the ζ does not become clockwise dominant until $t/\tau = 0.167$, and the development of ζ is much more gradual throughout (compare Figures 11a-f to Figures 11g-l). It is expected that the ζ should develop as a function of the model convective time scale, which is a larger fraction of the $k = 0.259$ pitching motion, leading to the difference in the developed ζ over phase, as well as the difference of the F_L vs. α_y and M_P vs. α_y paths in Figure 11.

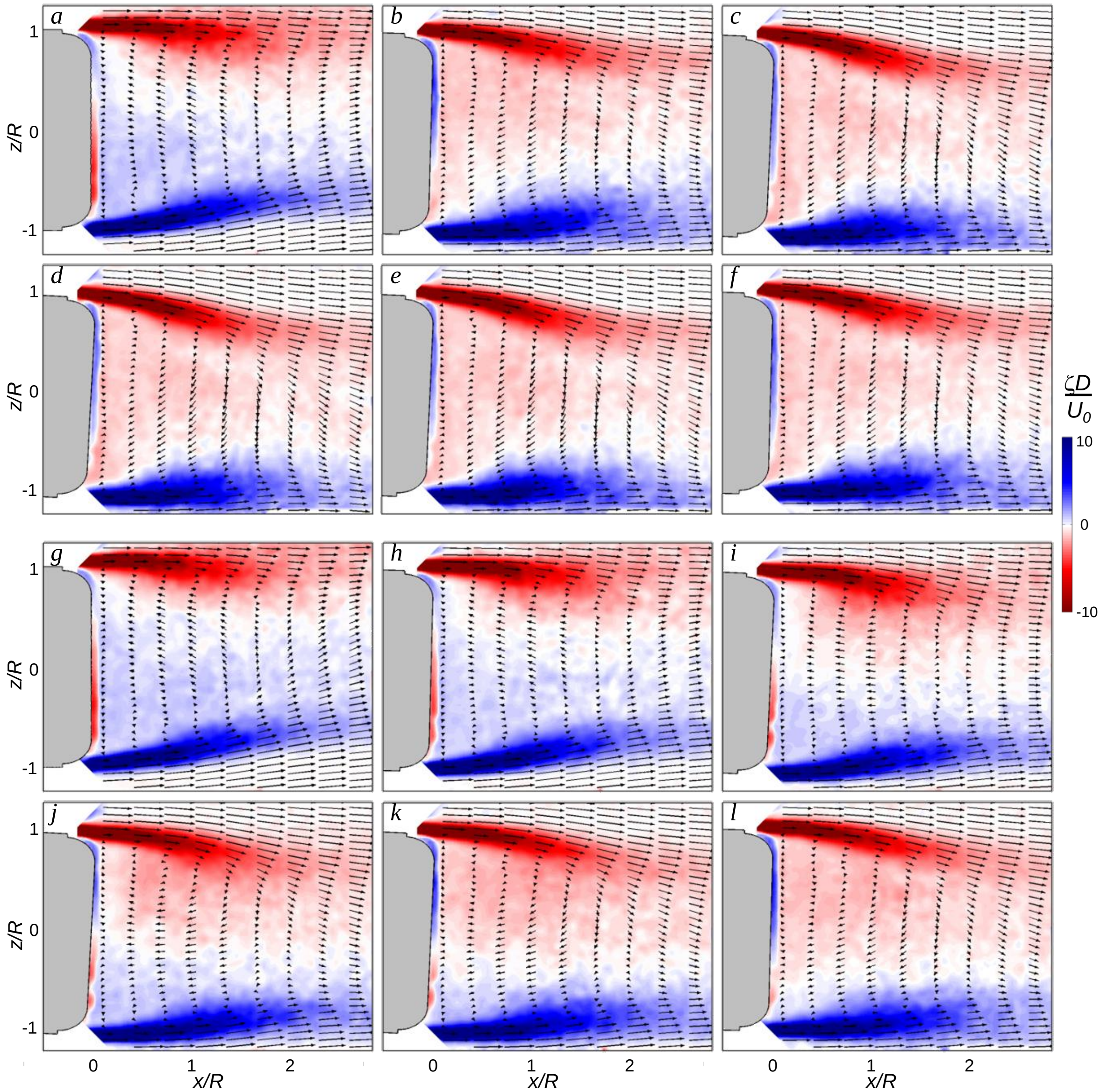

Figure 12. *Raster plots of the phase-averaged vorticity field with overlaid phase-averaged velocity vectors for $\alpha_y = \pm 3^o$ sinusoidal pitch at reduced frequencies of k = 0.013 (a-f), and 0.259 (g-l), at t/τ = 0 (a,g), 0.083 (b,h), 0.167 (c,i), 0.25 (d,j), 0.333(e,k), and 0.417(f,l).*

VI. Aerodynamic Force and Moment Control using Continuous Actuation

After the aerodynamic response from the body's baseline flow is assessed, the flow control actuation schemes are designed. To further understand the control authority of the hybrid actuation throughout a pitching cycle, the effect of continuous actuation by either the top or both the top and the bottom jets is examined over a range of k. The continuous actuation by a single (top) jet and dual (top and bottom) jets is shown in red and blue, respectively, in Figure 13 with the baseline response shown as a dotted line for reference. Figures 13a and e show the response at k = 0.013 with significant ΔF_L and ΔM_P by one jet throughout the cycle, with a maximum effect at α_y = -1°, in agreement with Figure 10a and c. When both jets are activated, the result is a F_L vs. α_y and M_P vs. α_y that is similar to the baseline case, showing that both jets impose equivalent but opposing effects and hence effectively cancel out the induced effect of each other. Figures 13b and f show the response at k = 0.065, where there are several noticeable differences from the lowest k = 0.013, where the F_L vs. α_y and M_P vs. α_y path of both the single top jet and two jets has changed. It is noteworthy that although the F_L vs. α_y and M_P vs. α_y paths have changed from the

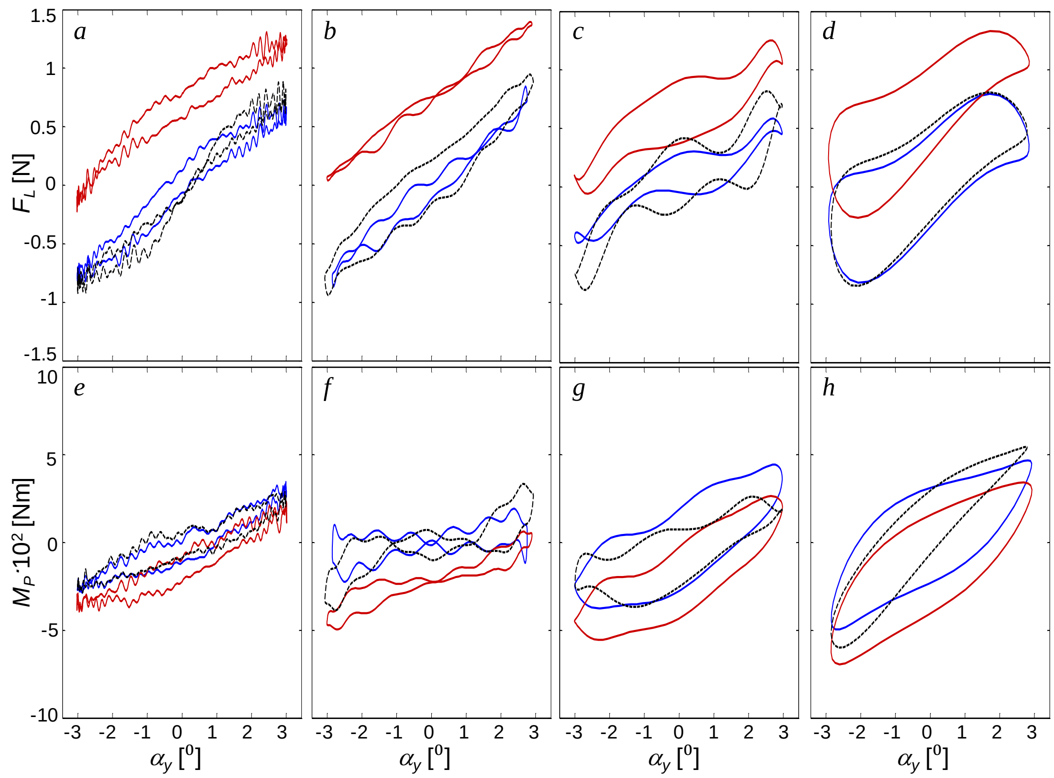

Figure 13. *Lift force (a-d) and pitching moment (e-h) for open-loop continuous activation of one (red) and both (blue) jets at $C_\mu = 3 \cdot 10^{-3}$ and k = 0.013 (a,e), 0.065 (b,f), 0.130 (c,g), and 0.259 (d,h). The non-actuated cases are shown in dashed (black) lines.*

lower frequency, the continuous actuation traces remain similar to the baseline paths, with the top jet path deflected to a larger F_L and lower M_P and the both jets path centered about the baseline paths. This trend continues in $k = 0.130$ (shown in Figures 13c and g) and $k = 0.259$ (shown in Figures 13d and h) with the actuated paths remaining similar to the non-actuated paths, and the activation of one jet causing a deflection of the path, with the largest variation occurring in the F_L vs. α_y path at $k = 0.130$ (Figure 13c). It is also noteworthy that at the frequencies $k = 0.065$ and 0.130 the actuation effect changes to an induced $\Delta F_L = 0.6$N and $\Delta M_P = -0.02$Nm approximately independent of α_y (Figures 13b,c,f and g) rather than an effect of $\Delta F_L = 0.9$N and $\Delta M_P = -0.01$Nm at a maximum $\alpha_y = -1^o$ in the 'low' frequency of $k = 0.013$ (Figures 13a and e). This change is attributed to the model moving fast enough that the flow doesn't have enough time to fully respond to the 'small' geometry of the backward facing step, and there is no longer a dependence between the pitching angle and this local geometry. In the 'high' frequency case $k = 0.230$ again starts to vary with α_y, having a maximum effect of $\Delta F_L = 0.5$N and $\Delta M_P = -0.015$Nm at $\alpha_y = 3^o$ (Figure 13 d and h). The emergence of this maximum at $\alpha_y = 3^o$ at $k = 0.259$ is attributed to the model moving fast enough such that the flow cannot fully respond to the model dynamic cycle, and therefore some parts of the pitching cycle become more favorable for actuation than other parts due to the altered shear layer dynamics. It is notable that the hysteresis in both the baseline and actuated responses in Figure 13 increases with oscillation frequency past $k = 0.065$, which is due to the flow development (function of τ_{conv}) taking up a larger percentage of the cycle, τ, but the nature of the flow development (hence path of F_L and M_P) is similar for the baseline and actuated cases with a fixed frequency. Although the actuation effects differ for different frequencies, it is important to note that this continuous actuation has a sizable effect across all the pitch frequencies tested, causing an average deflection on the order of $\Delta F_L \sim 0.6$N and $\Delta M_P \sim -0.01$Nm with one jet, and effectively cancelling this deflection with both jets, and preserving similar F_L vs. α_y and M_P vs. α_y paths with respect to the baseline flow in all cases.

To understand the similarity of the actuation-induced wake development with frequency while the axisymmetric model is pitching with an amplitude of 3°, the baseline, top jet, and both jets continuous actuation flow fields are investigated with planar time-averaged PIV. Figure 14 shows the time-averaged flow field (based on 500 individual flow realizations) in terms of the mean velocity field vectors overlaid on a raster plot of ζ, at the central vertical

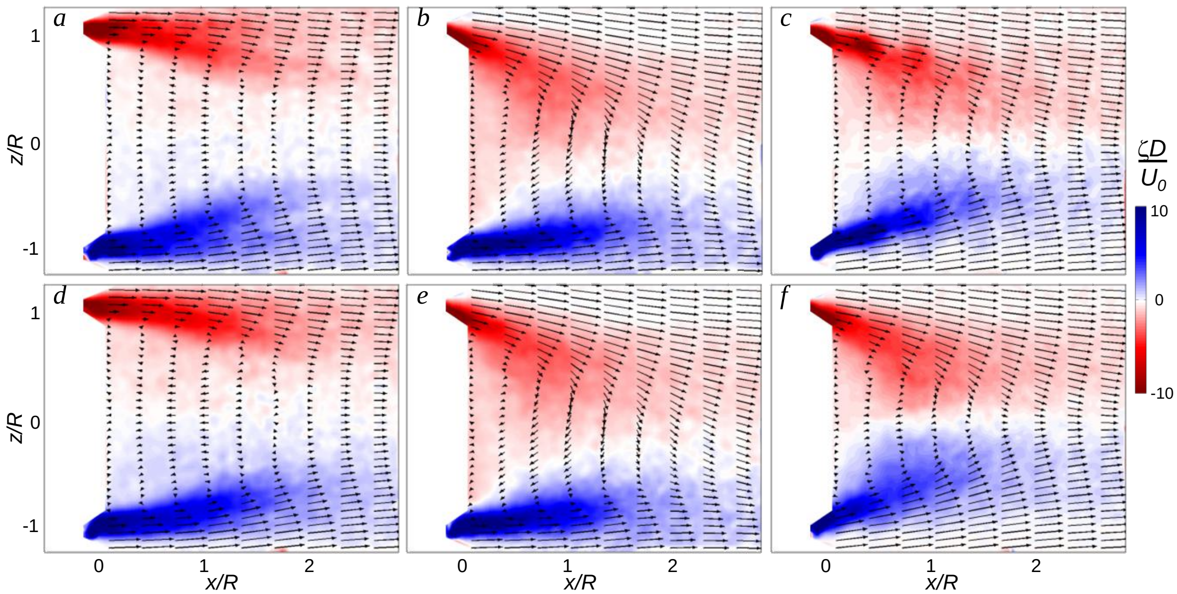

Figure 14. *Raster plots of the time-averaged vorticity field with overlaid time-averaged velocity vectors for $\alpha_y = \pm 3^0$ for non-actuated baseline (a,d), and the flow controlled by top (b,e), and both (c,f) jets for k = 0.013 (a-c) and 0.259 (d-f) at $C_\mu = 3\cdot 10^{-3}$.*

plane of the model. Figures 14 a-c show the model wake with $k = 0.013$, and Figures 14 d-f show the model wake with $k = 0.259$. Figures 14a and d show the model wake without flow control, having expected symmetry about the body's axis of symmetry, and remaining similar to Figure 9a when the model was held stationary, with an added diffusion of the shear layer originating from the dynamic motion of the model. The similarity between Figure 14a and Figure 14d suggest that the shear layer deflection magnitude is similar regardless of pitching frequency, with the major difference being the phase lag of the wake response, which is observed in Figure 12. Figure 14b shows the model wake with the top jet actuated, deflecting the wake downwards across the centerline and inducing a large asymmetry while decreasing the extent and magnitude of the region of ζ near the jet, analogous to Figure 9b. Figure 14c shows both jets activated, causing the extent and magnitude of the region of ζ near each jet to decrease, and vectors the wake on both side closer to the center, thereby closing the wake, analogous to Figure 9c. The similarity between Figures 14b and e with Figure 9b, and Figures 14c and f with Figure 9c, suggest that the shear layer deflection with jet actuation is also similar regardless of pitching frequency, which also suggests ΔF_L vs. α_y and ΔM_P vs. α_y is comparable to F_L vs. α_y and M_P vs. α_y.

VII. Aerodynamic Force and Moment Control using Modulated Actuation

Results shown in Figures 13 and 14 clearly demonstrates that the hybrid actuation approach has a significant control authority throughout the full range of the pitching dynamics $0 < k < 0.259$. The main objective of the present study is to apply such a control approach to control the aerodynamic forces (F_L vs. α_y and M_P vs. α_y paths) on the body undergoing dynamic pitch. It should be noted that the decrease of M_P growth with α_y can be used to stabilize the model, and increasing the M_P growth with α_y can be used to accelerate steering. This is a coupled system where the baseline F_L and M_P are both increasing with α_y, yet the ΔF_L and ΔM_P by the actuators are in opposite senses, therefore increasing growth of M_P vs. α_y (for accelerated steering) simultaneously reduces growth of F_L vs. α_y, and likewise decreasing growth of M_P vs. α_y (for stabilization) simultaneously increases growth of F_L vs. α_y. As it is assessed from Figure 13, the control authority ΔF_L relative to the baseline path of F_L was larger than ΔM_P relative to the baseline path of M_P, and therefore it is chosen to focus the flow control on augmentation of the F_L vs. α_y path as a case that can be used for stabilization, and cancellation of the F_L vs. α_y path as a case that can be used for accelerated steering. As it was found previously by Lambert et al.[24], the ΔF_L and ΔM_P induced by an equivalent synthetic jet varied linearly with $C_\mu < 3\cdot 10^{-3}$, and such a relationship is utilized in the current control scheme. Modulation commands, M_{TOP} and M_{BOT}, are tailored for each jet to each of the baseline force responses of Figure 11a-d with a jet momentum of $C_\mu = 3\cdot 10^{-3}$ corresponding to 100% modulation, which is commensurate with

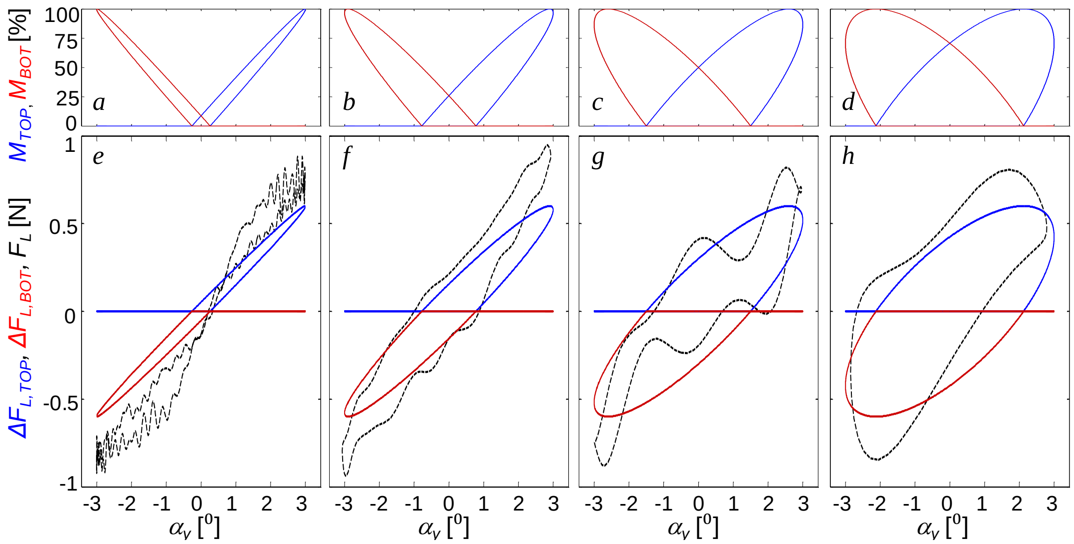

Figure 15. *Synthetic jet modulation schemes for force augmentation (a-d), and estimated actuator induced force (e-h) with top jet in blue and bottom jet in red for k = 0.013 (a,e), 0.065 (b,f), 0.130 (c,g), and 0.259 (d,h). The non-actuated force response is shown in dashed black. The modulation schemes for force cancellation are 180 ^{0} out of phase.*

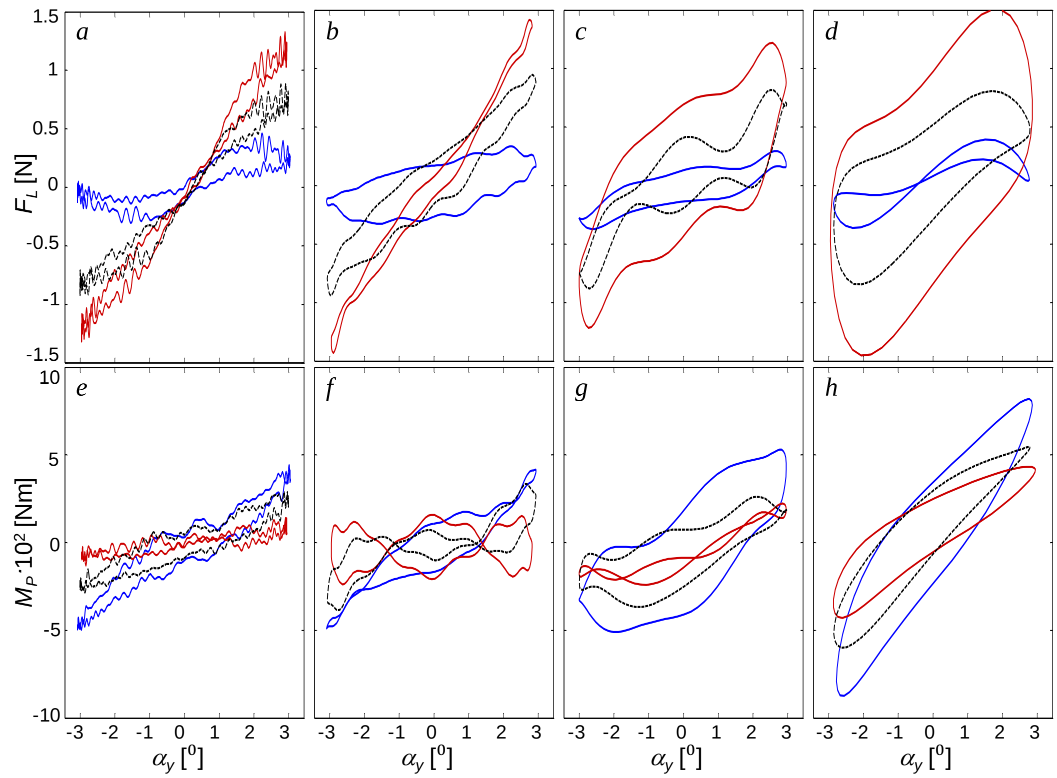

Figure 16. *Lift force (a-d) and pitching moment (e-h) for aerodynamic force cancellation (blue) and augmentation (red) with k = 0.013 (a,e), 0.065 (b,f), 0.130 (c,g), and 0.259 (d,h). Baseline responses are shown in dashed black.*

a ΔF_L ~ 0.6N, based on Figure 13. Figure 15a-d shows the resultant jet modulation signals with varying k = 0.013 (Figure 15a), 0.065 (Figure 15b), 0.130 (Figure 15c) and 0.259 (Figure 15d), where the only free parameter of variation used was the phase of the modulation signals. Here the top jet is shown in blue and the bottom jet is shown in red for force augmentation, although the modulation command for force cancellation can be generated by running the jets in the opposite fashion with the top jet in red and the bottom jet in blue. The corresponding predicted augmented ΔF_L using a maximum ΔF_L ~ 0.6N at 100% jet modulation for each jet, $\Delta F_{L,TOP}$ and $\Delta F_{L,BOT}$, are shown in Figure 15e-f for these same values of k. The phase of these modulation commands was chosen such that the predicted augmented F_L is most similar to the baseline F_L, leading to the chosen modulation command phase lags of 5° (k = 0.013, Figure 15a and e), 15° (k = 0.065, Figure 15b and f), 25° (k = 0.130, Figure 15c and g), and 40° (k = 0.259, Figure 15d and h), relative to α_y.

The results of the augmentation control schemes, as described in Figure 15, and the corresponding out of phase cancellation schemes, are shown in Figure 16 in red and blue, respectively, with the baseline response overlaid in a dashed line. The response of F_L vs. α_y is shown in Figures 16a-d, and the response of M_P vs. α_y is shown in Figures16e-h with varying k. At the lowest k = 0.013 (Figure 16a), the maximum F_L is cancelled to 0.45 N or augmented to 1.3 N from its baseline value of 0.9 N, leading to a 50% decrease or a 45% increase in the force peaks. The respective case of M_P vs. α_y in Figure 16e shows a 30% increase which can be used for model steering authority and a 65% decrease in the moment peaks which can be used for model stabilization authority. For k = 0.065 (Figure 16b and f), the F_L augmentation case leads to a 55% increase in F_L with a 50% decrease in M_P, and the F_L cancellation case leads to a F_L decrease of 65% and an M_p increase of 33%. Overall, the control authority on the F_L vs. α_y increased and M_P vs. α_y decreased from k = 0.013 to 0.065. At k = 0.130 (Figure 16c and g), the control authority on F_L decreases slightly from k = 0.065, with a 50% increase and a 60% decrease, and the control authority on M_P becomes the respective 20% decrease and a 55% increase. The resulting F_L vs. α_y cancellation and augmentation effects remain significant at k = 0.259 (Figure 16d and h), with induced changes on F_L of a 105% increase and a 50% decrease, with the respective changes on M_P of a 20% decrease and a 40% increase. For the two lowest k (Figure 16a,b,e,and f) the cancelled and augmented paths show a hysteresis comparable to the baseline flow, but for k > 0.065 (Figure 16c,d,g, and h), the cancellation of F_L vs. α_y decreases the force path hysteresis (decreases the lift response time relative to the cycle), and the augmentation of the F_L vs. α_y increases the force path hysteresis (increases the lift response time relative to the cycle). It is noteworthy that the hysteresis in M_P vs. α_y is of the opposite sense to the force, and therefore increasing the hysteresis of the F_L vs. α_y decreases the hysteresis of the M_P vs. α_y path, and vice versa.

The 'low' frequency oscillation flow control cases are analyzed in detail with the phase-averaged flow fields measured by PIV. Figure 17 shows six phase-averaged flow fields (based on 300 individual phase-referenced realizations) in terms of the velocity field vectors overlaid on a raster plot of ζ, at the central vertical plane of the model for k = 0.013 (τ = 1s) with the F_L vs. α_y cancellation (Figure 17a-f), and augmentation (Figure 17g-l). Similar to the baseline cycle, both the cancellation and augmentation actuation flow fields are symmetric across the pitching cycle, and therefore the phases chosen for brevity are representative for the first half cycle, similar to Figure 12: t/τ = 0 (Figure 17a and g), 0.083(Figure 17b and h), 0.167(Figure 17c and i), 0.25(Figure 17d and j), 0.333(Figure 17e and k), and 0.417(Figure 17f and l). Based on Figure 15, the actuation chosen for this value of k lags α_y in phase by 5°. In Figure 17a, α_y has reached 0° and the top jet is weakly actuated. As the model pitches up to 3° in Figure 17b-d, the bottom actuation is activated and increases in strength, causing the domain of counterclockwise ζ to increase, and the actuation then decreases from 17d-f, causing the domain of counterclockwise ζ to decay. The presence of actuation in Figure 17a-f causes the location of zero ζ to remain closer to the centerline and causes the velocity field to remain more symmetric about the centerline compared to the baseline flow (compare Figure 17a-f with Figures 12a-f), commensurate with the smaller peaks observed in the F_L vs. α_y path in Figure 16a. For F_L vs. α_y augmentation (Figure 17g-l), the opposite modulation command to the actuators is sent. Initially in Figure 17g, the bottom actuator is active, and between the next phase shown in Figure 17h the bottom actuator is terminated and the top actuator is activated. The top actuator's strength increases from Figure 17h-j and then decreases from Figure 17j-l. The presence of actuation in Figure 17g-l causes the location of zero ζ to deflect farther from the centerline and causes the velocity field to remain less symmetric around the centerline compared to the baseline flow (compare Figure 17g-l with Figures 12a-f), commensurate with the enhanced peaks observed in the F_L vs. α_y path in Figure 16a.

To further understand the time varying 'low' frequency wake dynamics of both the controlled and uncontrolled flows, the time development of streamwise velocity, u_x, cross-stream velocity, u_z, and the planar vorticity, ζ in the wake behind the model is assessed. These quantities are characterized at a representative fixed downstream distance of x/R = 1 behind the model aft end for 0 < t/τ < 1. Figure 18a shows the development of the u_x component of the wake velocity when there is no actuation present, where u_x responds to sinusoidal pitch cycle. The u_z component of the wake velocity is shown in Figure 18d, where u_z is mostly downward for t/τ < 0.5, corresponding to the wake

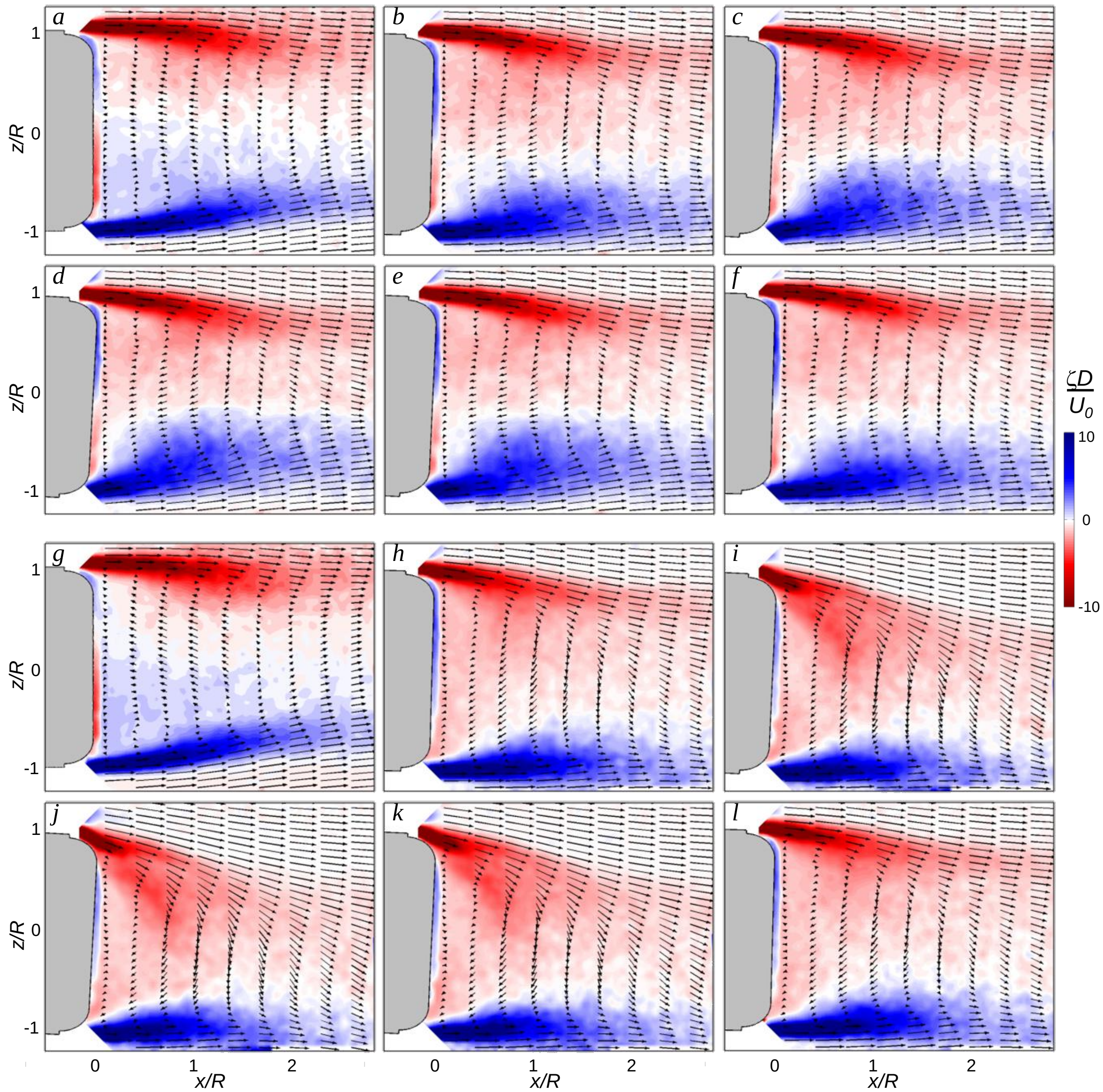

Figure 17. *Raster plots of the phase-averaged vorticity field with overlaid phase-averaged velocity vectors for $\alpha_y = \pm 3^0$ sinusoidal pitch at reduced frequency k = 0.013 using force cancellation (a-f), and augmentation (g-l) at t/τ = 0 (a,g), 0.083 (b,h), 0.167 (c,i), 0.25 (d,j), 0.333(e,k), and 0.417(f,l).*

following the model and being vectored downward when $\alpha_y > 0$, and mostly positive for $t/\tau > 0.5$, which corresponds to the wake being vectored by the model upward when $\alpha_y < 0$. Figure 18g shows the development of ζ for the baseline flow, which also, as expected, follows a sinusoidal path similar to u_x. Upon F_L vs. α_y cancellation actuation, the wake's variation in u_x decreases significantly throughout the cycle from the baseline, as shown in Figure 18b, and conversely, the wake's variation in u_x increases significantly with the F_L vs. α_y augmentation actuation, as shown in Figure 18c. There is a different effect in the vertical direction, where F_L vs. α_y cancellation (Figure 18e) causes the magnitude of the u_z to decrease significantly across the entire region throughout all times, and the F_L vs. α_y augmentation (Figure 18f) enhances the u_z development seen in Figure 18d. The response of ζ to F_L vs. α_y cancellation is shown in Figure 18h, with a growth in the area of the shear layer upon actuation, with the bottom actuator present for $t/\tau < 0.5$ and the top actuator present for the other half of the cycle. There is a notable decrease in the deviation of the zero level of ζ with time that was observed in Figure 17a-f, which is commensurate with the decreased force measured in Figure 16a. The ζ response to F_L vs. α_y augmentation instead involves a strong

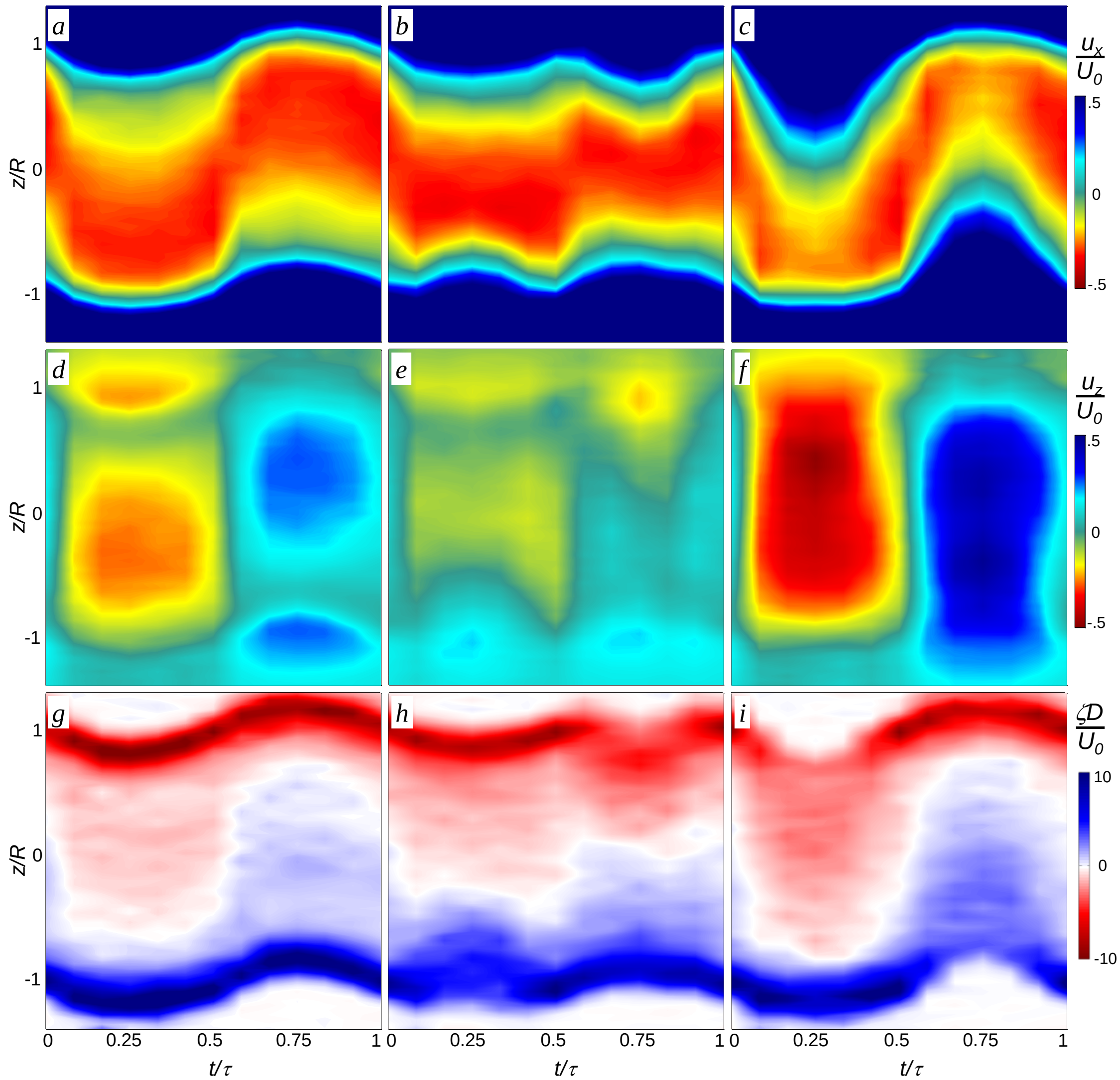

Figure 18. *Time development of streamwise (a-c) and cross-stream (d-f) velocity and vorticity (g-i) at a streamwise location of x/R = 1 from the model aft end for α_y = ±3 ^{o} sinusoidal pitch at reduced frequency of k = 0.013, without actuation (a,d,g), and for the force cancellation (b,e,h) and augmentation (c,f,i).*

vectoring and spreading of the shear layer and an increase in the ζ found in the wake, which increases the deviation of the zero level of ζ in the wake, commensurate with the augmentation of force measured in Figure 16a.

The 'high' frequency, k = 0.259, oscillation flow control cases are also analyzed in detail with the phase averaged flow field measured by PIV, and represented in the same fashion as Figure 17, over half of the pitching cycle. Based on Figure 15, the actuation chosen for this value of k lags α_y in phase by 45°. In Figure 19a, α_y has reached 0° and the top jet is moderately actuated. As the model pitches up through Figures 19a-b ($0 < t/\tau < 0.083$), the top actuation is decreased, and transitions to the bottom jet, with increasing intensity in Figure19c-e ($0.167 < t/\tau < 0.333$). Between Figures 19e-f ($0.333 < t/\tau < 0.417$), the bottom actuation begins to decrease. It should be noted that although the modulation at this 'high' frequency lags the modulation at the 'low' frequency by 40°, the flow observed through Figures 19a-f remains more symmetric then the baseline cases shown in Figure 12g to Figure 12l. This is owing to the aerodynamic force and moment response on the model also inherently lagging the model motion with a similar delay. For 'high' frequency F_L vs. α_y augmentation (Figure 19g-l), the opposite modulation command to the actuators is sent as in Figure 19a-f. Initially, the model shear layer is deflected upward as it is lagging the model position, and the bottom jet is moderately actuated in Figure 19g. As the model pitches up through Figures 19g-i ($0 < t/\tau < 0.167$), the bottom actuation is terminated and transitions to increasing top actuation

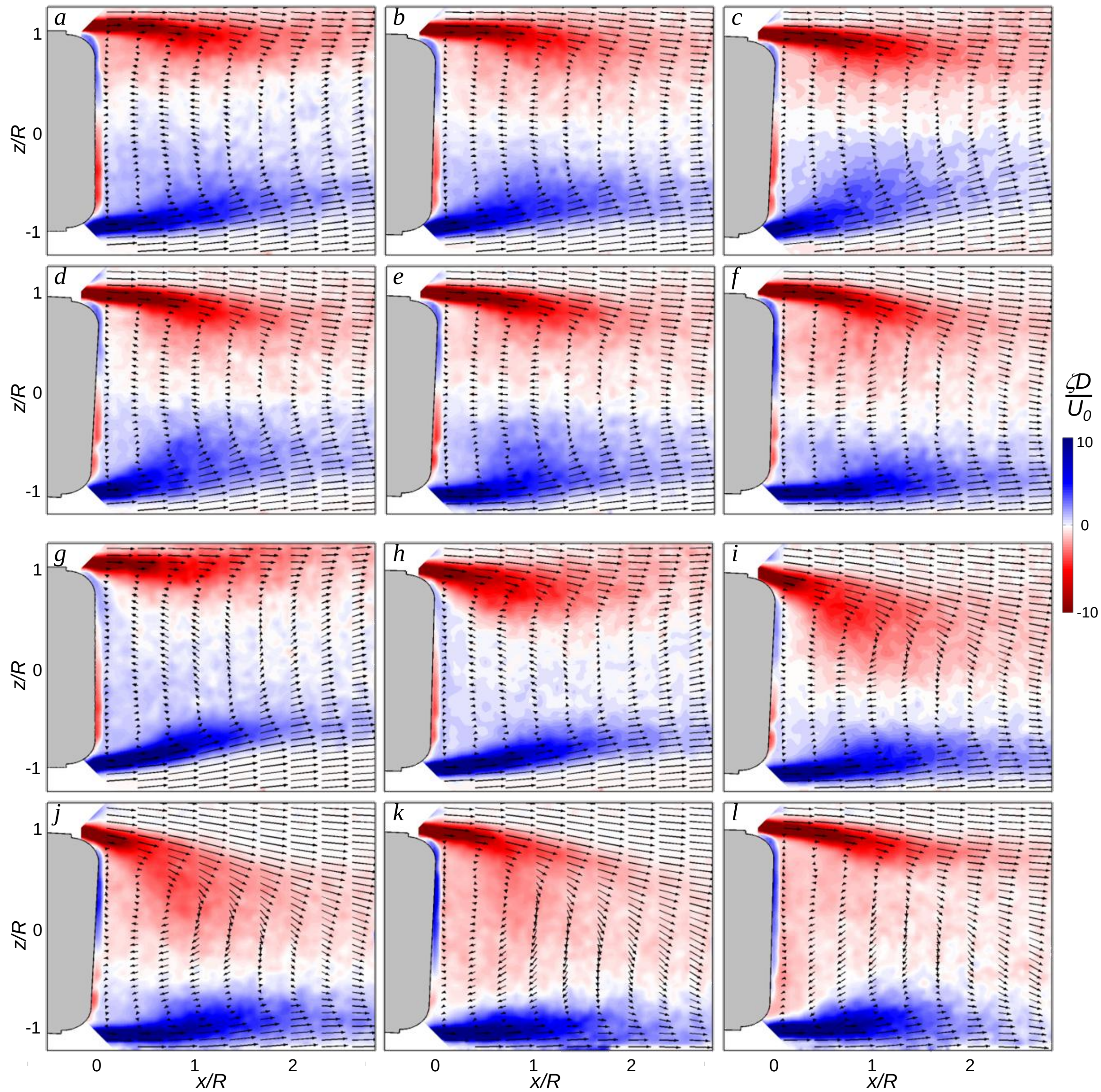

Figure 19. *Raster plots of the phase-averaged vorticity field with overlaid phase-averaged velocity vectors for $\alpha_y = \pm 3^{o}$ sinusoidal pitch at reduced frequency of $k = 0.259$ using force cancellation (a-f), and augmentation (g-l) at $t/\tau = 0$ (a,g), 0.083 (b,h), 0.167 (c,i), 0.25 (d,j), 0.333(e,k), and 0.417(f,l).*

in Figures 19c-e ($0.167 < t/\tau < 0.333$). In the time instances shown in Figures 19e-f ($0.333 < t/\tau < 0.417$), the modulation of the top actuation is reduced. Comparing Figures 19g-l and Figures 12g-l show the increased time of transition of the wake ζ, is commensurate with the growth of hysteresis in Figure 16d, as well as the increased extent of the shear layer is commensurate with the growth of the F_L peaks during actuation.

A detailed investigation analogous to the 'low' frequency pitch oscillations is conducted at the highest k to gain a better understanding of the 'high' frequency wake dynamics of the F_L vs. α_y cancellation and augmentation, and their similarities and differences to the 'low' frequency case. To do this, the time development of u_x, u_z, and ζ are presented for the 'high' frequency $k = 0.259$, showing the same comparisons as for the 'low' $k = 0.013$ (Figure 18). Figure 20a shows the development of u_x when there is no actuation present, where u_x responds as a sinusoid with the same ~45° phase lag behind α_y. Figure 20d shows u_z development in the baseline flow, with a different structure than what was observed in the lower frequency case in Figure 18d. Here, u_z is mostly downward when u_x is deflected downward, and u_z is mostly upward when u_x is deflected upward, showing the same ~45° phase lag from

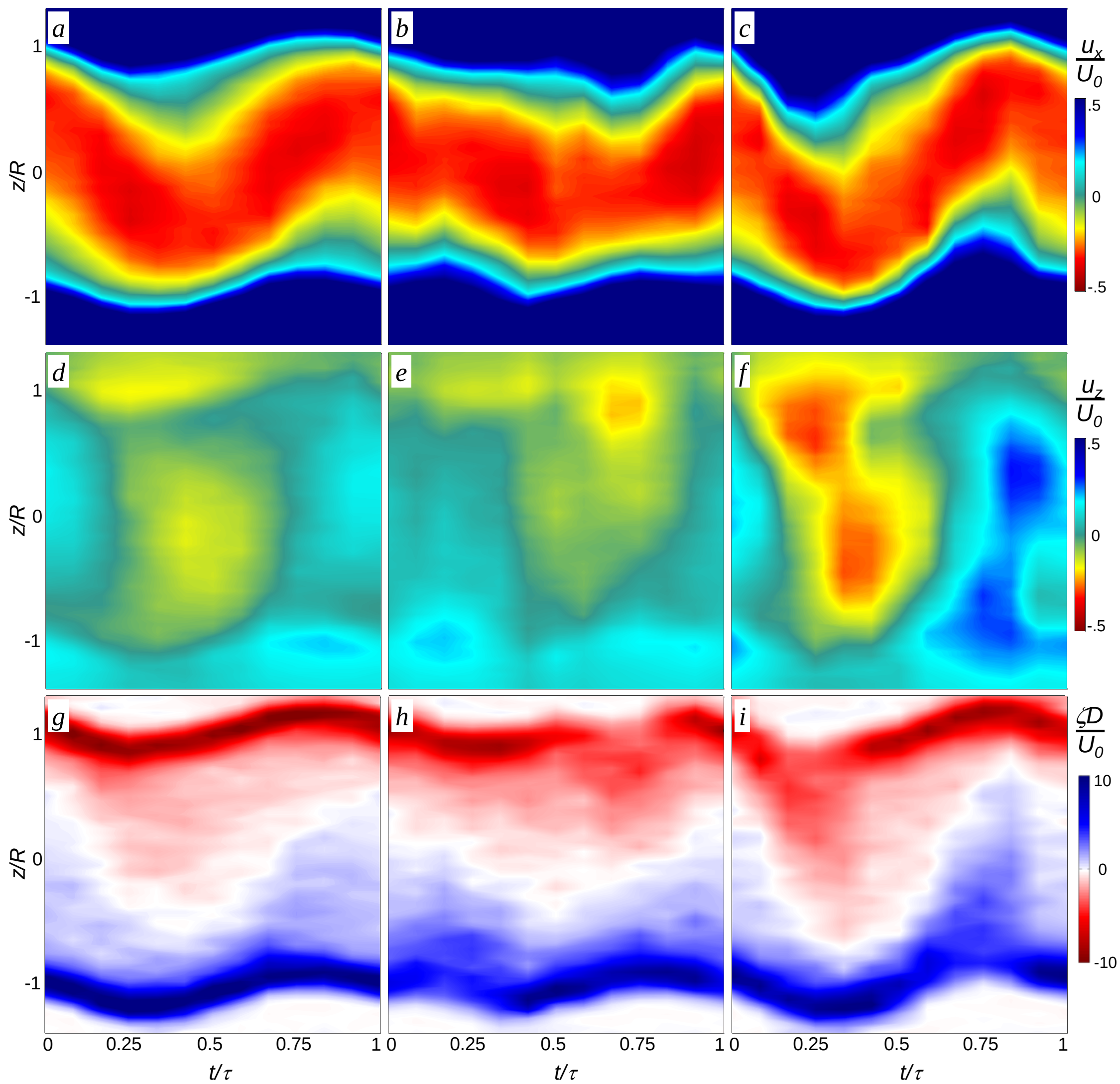

Figure 20. *Time development of streamwise (a-c) and cross-stream (d-f) velocity and vorticity (g-i) at a streamwise location of x/R = 1 from the model aft end for $\alpha_y = \pm 3^{\,o}$ sinusoidal pitch at reduced frequency of k = 0.259, without actuation (a,d,g), and for the force cancellation (b,e,h) and augmentation (c,f,i).*

α_y observed in u_x. It is also notable that the magnitude of the baseline u_z is significantly smaller at this higher frequency (compare 18d and 20d). The baseline ζ development over the pitching cycle is shown in Figure 20c, which follows α_y with ~45° phase lag in agreement with the streamwise and vertical velocity components. The structure of the ζ agrees well with the structure observed in the 'low' k pitching. Upon F_L vs. α_y cancellation actuation, the wake's variation in u_x decreases significantly throughout the cycle from the baseline, as shown in Figure 20b, and conversely, the wake's variation in u_x increases significantly with the F_L vs. α_y augmentation actuation, as shown in Figure 20c, in the same fashion as k = 0.013, with the exception that u_x now lags the model motion (compare Figures 20a-c with Figures 18a-c). At this 'high' frequency oscillation, there is a smaller effect in the vertical direction, compared to low frequencies, where F_L vs. α_y cancellation (Figure 20e) does not change the magnitude of u_z, but instead slightly delays its development in time. The F_L vs. α_y augmentation (Figure 20f) dominates the baseline u_z development seen in Figure 20d, and causes an increase in magnitude of u_z. The response of ζ to F_L vs. α_y cancellation is shown in Figure 20h, which manipulates the sense of ζ such that the region of zero ζ remains close to the centerline. Comparing Figure 20h to Figure 18h, the suppression of the vertical range of zero ζ is fundamentally similar, but the shear layer spreading is reduced. Although the structure is somewhat different, as the vertical range of zero ζ is still suppressed, the corresponding F_L vs. α_y on the body is also successfully reduced.

The ζ response to F_L vs. α_y augmentation (Figure 20i) instead involves an increase in the ζ in the wake, which increases the deviation of the zero level of ζ in the wake, commensurate with the augmentation of force measured in Figure 16d. The two major differences between Figure 20i and Figure 18i are the phase lag of the response of the wake, and the reduced spreading of the shear layer.

VIII. Conclusions

The present experimental work is focused on fluidic flow control applications to a moving aerodynamic platform, and coupling to and altering of the resulting aerodynamic forces and moments. The flow control concepts are demonstrated on an axisymmetric model having a prescribed sinusoidal pitch oscillations at a range of reduced frequencies $0 < k < 0.259$. In contrast to the prior work by Lambert et al.[25], where the flow control was applied to either suppress or augment a body motion which was free to oscillate under the aerodynamic moment in a single degree of freedom system, this study focuses on control of the motion-induced aerodynamic forces and moments while the body's dynamic path is prescribed and preserved. For that purpose, a novel six degree of freedom traversing system is designed and implemented.

The wind-tunnel model is suspended by eight wires with custom servo actuators utilized to control the end points and tensions in each wire. This mechanism is designed to move all the wires in patterns that can cause rotation in three independent axes: roll (±8°), pitch (±15°), and yaw (±9°), as well as the respective independent translations: streamwise, cross-stream, and vertical, all within a range of ±50 mm. Each wire has an incorporated load cell that resolves the tension, and thereby captures the aerodynamic forces and moments on the model. Motion is executed by an in-house real-time PID controller that provides signals to the servo actuators as commanded. The executed motion is recorded by an external six degree of freedom *Vicon* camera system (515 fps), which output is fed into the controller as a feedback signal to maximize the accuracy of motion. The real-time control system utilizes two *Quanser* data acquisition boards.

The traverse-driven model motion is tested in multiple degrees of freedom, and it could generate desired complex trajectories, comprised of the combined translational and rotational motions. These trajectories could be realized with minimal error compared to the commanded motion, being executed in a PID control loop having feedback from the motion analysis system. In the present work, the flow control capabilities are demonstrated on the model undergoing sinusoidal pitch oscillations. The flow control is effected by either continuous or modulated activation of two synthetic jets that emanate from narrow, azimuthally-segmented slots on the model's aft end, opposite to each other at its top and bottom surface. This main active flow control component is assisted by passive modifications of the surface geometry that involve a short backward-facing step and trailing Coanda surface, and this tandem utilization of active and passive flow control is often coined as 'hybrid' flow control. The flow control actuation effects by the synthetic jets are assessed relative to the lift force and pitch moment induced on the model when it is held stationary at center, as well as when it is commanded to pitch dynamically.

As the pitch-induced aerodynamic force and moment on the body are of the same sense and the pitch-induced moment acts to further increase the pitch angle, this baseline moment is essentially 'unstable'. In contrast, the actuation by either top or the bottom jet induces a normal force and moment of opposite signs. Hence, depending on which jet is activated, flow control is utilized to either suppress the aerodynamic moment (and augment the force) or augment the moment (and suppress the force). These actuation realizations are then implemented into an open-loop flow control scheme with adjustable phase offset of actuation relative to the model's period of oscillation. The resulting suppressed/enhanced pitch moment/lift force (and vice versa) flow control schemes are executed during the sinusoidal pitch motion, indicated a robust flow control effect over the full range of the pitch frequencies ($0 < k < 0.259$). Typical alteration of the aerodynamic force and moment was approximately 50% of the uncontrolled levels. It is argued that these flow control schemes can be utilized for accelerated steering or stabilization of an equivalent airborne body.

Acknowledgment

This work has been supported by the Army Research Office monitored by Dr. Frederick Ferguson.

References

[1]Wu, J.-Z., Lu, X.-Y., Denny, A. G., Fan, M., and Wu, J.-M., "Post Stall Flow Control on an Airfoil by Local Unsteady Forcing," *Journal of Fluid Mechanics*, Vol. 371, 21-58, 1998.

[2]Hsiao, F. B., Liu, C. F., and Shyu, J. Y., "Control of Wall-Separated Flow by Internal Acoustic Excitation", *AIAA J.*, Vol. 28, 1990, pp. 1440-1446.

[3]Neuberger D. and Wygnanski I., "The Use of a Vibrating Ribbon to Delay Separation on Two Dimensional Airfoils", Proceedings of Air Force Academy Workshop in Unsteady Separated Flow (Colorado Springs, CO), F.J Seiler, ed., Report TR-88-0004, 1987.

[4]Williams, D., Acharya, M., Bernhardt, K. & Yang, P., "The Mechanism of Flow Control on a Cylinder with the Unsteady Bleed Technique", *AIAA Paper 1991-0039*, 1991.

[5]Chang, R. C., Hsiao, F. B., and Shyu, R. N., "Forcing Level Effects of Internal Acoustic Excitation on the Improvement of Airfoil Performance", *J. Aircraft,* Vol. 29, 1992, pp. 823-829.

[6]Seifert, A., Bachar, T., Koss, D., Shepshelovich, M. and Wygnanski, I., "Oscillatory Blowing: A Tool to Delay Boundary-Layer Separation", *AIAA J.,* Vol. 31, 1993, pp. 2052-2060.

[7]Erk, P. P., "Separation Control on a Post-stall Airfoil using Acoustically Generated Perturbations", PhD Thesis, Tech. Univ. Berlin, Germany, 1997.

[8]Smith, D. R., Amitay, M., Kibens, V., Parekh, D., and Glezer, A., "Modification of Lifting Body Aerodynamics Using Synthetic Jet Actuators", *AIAA Paper* 1998-0209, 1998.

[9]Amitay, M., Smith, D. R., Kibens, V., Parekh, D. E., and Glezer, A., "Aerodynamic Flow Control over an Unconventional Airfoil Using Synthetic Jet Actuators", *AIAA J.***,** Vol. 39, 2001, pp. 361-370.

[10]Honohan, A. M., Amitay, M., and Glezer, A., "Aerodynamic Control using Synthetic Jets", *AIAA Paper* 2000-2401, 2000.

[11]Glezer, A., Amitay, M., and Honohan, A. "Aspects of Low- and High-Frequency Actuation for Aerodynamic Flow Control," *AIAA Journal*, Vol. 43, 1501-1511, 2005.

[12]Newman, B.G., "The Deflexion of Plane Jets by Adjacent Boundaries-Coanda Effect", *Boundary Layer and Flow Control Principles and Applications,* Vol. 1, 1961, pp. 232-264.

[13]Englar, Robert J., "Circulation Control Pneumatic Aerodynamics: Blown Force and Moment Augmentation and Modification; Past, Present, & Future", AIAA Paper 2000-2541.

[14]Sigurdson. L. W., "The Structure and Control of a Turbulent Reattaching Flow", *J. Fluid Mech*., Vol. 298, 1995, pp. 139-165.

[15]Nagib, H. M., Reisenthel, P. H., and Koga, D. J. "On the Dynamical Scaling of Forced Unsteady Flows", *AIAA Paper* 1985-0553, 1985.

[16]Lo, K. P., Elkins, C. J., Eaton, J. K., "Separation Control in a Conical Diffuser with an Annular Inlet: Center Body Wake Separation", Exp. Fluids, Vol 53, 2012, pp 1317-1326.

[17]Freund, J. B., Mungal, M. G., "Drag and Wake Modification of Axisymmetric Bluff Bodies Using Coanda Blowing", *J. Aircraft,* Vol. 31, 1994, pp. 572-578

[18]Rinehart, C., McMichael, J. M., and Glezer, A., "Transitory Flow and Force Development on a Body of Revolution Using Synthetic Jet Actuation", *AIAA Paper* 2003-0618, 2003.

[19]Rinehart, C., "Aerodynamic Forces Induced by Controlled Transitory Flow on a Body of Revolution", Ph. D. Thesis, Georgia Institute of Technology, 2011.

[20]Corke, T. C., Tillotson, D., Patel, M. P., Su, W. J., Toldeo, W., "Radius Flow Vectoring for Projectile Drag and Steering Control Using Plasma Actuators", *AIAA Paper* 2008-3769, 2008.

[21]McMichael, J., Lovas, A., Plostins, P., Sahu J., Brown, G., and Glezer, A., "Microadaptive Flow Control Applied to a Spinning Projectile", *AIAA Paper* 2004-2512, 2004.

[22]Abramson, P., Vukasinovic, B, and Glezer, A., "Direct Measurements of Controlled Aerodynamic Forces on a Wire-suspended Axisymmetric Body", *Exp. Fluids,* Vol. 50, 2011, pp. 1711-1725.

[23]Abramson, P., Vukasinovic, B., and Glezer, A., Fluidic Control of Aerodynamic Forces on a Bluff Body of Revolution, *AIAA J.*, Vol. 50, pp.832-843, 2012.

[24]Lambert, T. J., Vukasinovic, B., and Glezer, A. "Unsteady Aerodynamic Flow Control of a Wire-Suspended, Moving Axisymmetric Body", *AIAA Paper* 2012-0073, 2012.

[25]Lambert, T. J., Vukasinovic, B., and Glezer, A. "Yaw Control of a Moving Axisymmetric Body using Synthetic Jets", *AIAA Paper* 2013-0106, 2013.

[26]Nicolaides, J. D., "A History of Ordnance Flight Dynamics", AIAA Paper *70-533*, 1970.

[27]Murphy, C. H., "Symmetric Missile Dynamic Instabilities", *AIAA J. Guidance and Control,* Vol. 4, No. 5, *80-0320R*, 1980.

[28]Price Jr., D. A., "Sources, Mechanisms, and Control of Roll Resonance Phenomena for Sounding Rockets.", *AIAA J. Spacecraft,* **4**, No. 11, 1516-1521, 1967.

[29]Murphy, C. H., "Some Special Cases of Spin-Yaw Lock In", US Army Ballistic Research Laboratory, BRL-MR-3609, 1987.

[30]Barrett, R. M., Lee, G. M., "Design and Testing of Piezoelectric Flight Control Actuators for Hard Launch Munitions," *Proc. SPIE* 5390, Smart Structures and Materials 2004: Smart Structures and Integrated Systems, 459, 2004.

[31]Sahu, J., "Time-Accurate Computations of Free-Flight Aerodynamics of a Spinning Projectile with and without Flow Control", AIAA Paper, 2006-6006.

[32]Ollerenshaw, D., Costello, M., "Model Predictive Control of a Direct Fire Projectile Equipped with Canards," *Journal of Dynamic Systems, Measurement, and Control*, Vol. 130, 2008.

[33]Ollerenshaw, D., Costello, M., "Simplified Projectile Swerve Solution for General Control Inputs," *Journal of Guidance, Control, and Dynamics*, Vol. 31, 1259-1265, 2008.

[34]Higuchi, H., Van Langen, P., Sawada, H., Timney, C. E., "Axial Flow Over a Blunt Circular Cylinder With and Without Shear Layer Reattachment", *J. Fluids Struct.*, Vol. 22, 1996, pp. 949-959.

[35]Hoerner, S. F., *Fluid-Dynamic Drag*, Hoerner Fluid Dynamics, Bricktown, New Jersey, 1965.